INTERNATIONAL JOURNAL FOR NUMERICAL METHODS IN FLUIDS
Int. J. Numer. Meth. Fluids 2003; **43**:1067–1079 (DOI: 10.1002/fld.509)

Modelling three-dimensional rotating flows in cylindrical-shaped vessels

K. S. Sujatha and M. F. Webster*,†

Institute of Non-Newtonian Fluid Mechanics, Department of Computer Science, University of Wales Swansea, Singleton Park, Swansea SA2 8PP, U.K.

SUMMARY

This paper reports on a study concerned with the numerical simulation of dough kneading that arises in the food processing industry. The flows considered are in a complex domain setting. Two dough mixers running at various rotation speeds are studied; one with a single stirrer and the other with two stirrers. Stirrers are fixed on the lid of the vessel and the motion is driven by the rotation of the outer vessel. Two different mixer orientations are considered, generating horizontal or vertical-rotating flow fields. Three-dimensional numerical simulations are performed on the full flow equations in a cylindrical polar co-ordinates system, through a finite-element, semi-implicit time stepping, Taylor–Galerkin pressure-correction scheme. The results reflect excellent agreement against the equivalent experimental findings. The motivation for this work is to develop advanced technology to model the kneading of dough. The ultimate target is to predict and adjust the design of dough mixers, so that optimal dough processing may be achieved notably, with reference to local rate-of-work input. Copyright © 2003 John Wiley & Sons, Ltd.

1. INTRODUCTION

This article reports on a study concerned with the numerical simulation of dough-kneading that occurs in food processing industry. Flow in a rotating cylinder is investigated when the fluid is mixed in a cylinder with a stirrer. There has been a considerable amount of studies on flow between eccentric rotating cylinders as that is appropriate to journal bearings. Background literature is heavily cited in the paper by Beris *et al.* [1], for which it is assumed that the fluid inertia is negligible and the clearance gap is small compared to the radii of the cylinders. However, in many practical applications, inertial effects are significant. Some of the relevant literature is cited below. Xue *et al.* [2] have simulated Newtonian and viscoelastic problems in three-dimensional time-dependent flow using an implicit finite volume formulation. They

* Correspondence to: M. F. Webster, Institute of Non-Newtonian Fluid Mechanics, Department of Computer Science, University of Wales Swansea, Singleton Park, Swansea SA2 8PP, U.K.
† E-mail: m.f.webster@swansea.ac.uk

Contract/grant sponsor: BBSRC; contract/grant number: 58/D08174

Received 3 March 2002
Revised 22 November 2002

focused on swirling flows in a confined cylinder with a rotating bottom lid. The suitability of different constitutive models for viscoelastic fluids is also discussed. Atobe [3] has reported chaotic motion of fluid particles in Stokes flow between two counter-rotating eccentric cylinders. Kim [4] has developed a mixed Galerkin technique with B-spline basis functions to compute two-dimensional incompressible flow between eccentric rotating cylinders. Dai *et al.* [5] examined the effects of coupling the equations of motion and energy by allowing variation in fluid viscosity with temperature, for flow between eccentric, rotating cylinders. Christie *et al.* [6] have analysed flow of a slightly non-Newtonian fluid between eccentric rotating cylinders. Prakash and Kokini [7–9] studied the shear-rate and velocity distribution in a model mixer using laser-doppler anemometry (LDA). They observed high shear-rates in the region near blades and the values ranged from 0 to 400 s^{-1}. Based on these data, an equation to predict shear-rate distribution in the model mixer was developed. Other researchers [10] have reported mean shear-rates ranging from 10 to 10^4 s^{-1}, in the mixer.

The present study is aimed at developing an algorithm to simulate the types of flow which are encountered in the food processing industry. In particular, those arising within the context of stirring and kneading of dough-based materials. Finite element methods for incompressible viscous flows have been implemented for dealing with non-Newtonian materials, under transient and isothermal conditions within a three-dimensional cylindrical polar co-ordinate system. The fluid material is driven by one or two stirrers, fixed to a lid that is placed upon a cylindrical vessel. The stirrers may be positioned in concentric or eccentric arrangement with respect to the axis of the vessel. As an alternative to conventional mixer protocol, the motion is assumed to be driven by the rotation of the vessel, as opposed to the stirrer, to avoid the complications arising from moving the stirrers through the mesh. Finally, we demonstrate how the equivalence in driven-motion may be established. The rotation path of the stirrers is about the center of the vessel. Both horizontal and vertical vessel orientations are considered to accommodate different types of stirring, as arise typically in biscuit or bread-producing processes. The quality of the final product, depends on the right balance of mechanical energy within the mixer. From the velocity profile, velocity gradients are estimated and then the local shear-rate values are calculated. From these data, the local rate-of-work done and torque are computed.

The simulation procedure addresses the numerical solution of the fully three-dimensional generalized Navier–Stokes equations for incompressible flows. This involves a so-called Taylor –Galerkin finite element formulation, which applies a temporal discretization in a Taylor series prior to a Galerkin spatial discretization. A semi-implicit treatment for diffusion is employed to address linear stability constraints. Full details on this scheme have already been published extensively in the References [11, 12]. The flow is modelled as incompressible, via a pressure-correction scheme. An inelastic model with shear-rate-dependent viscosity is incorporated, though this is extended to consider viscoelastic fluids elsewhere [13, 14].

2. GOVERNING EQUATIONS AND NUMERICAL SCHEME

For Newtonian and incompressible isothermal flow, the generalized momentum and continuity equations may be expressed as

$$\rho U_t = \nabla \cdot (\mu \nabla U) - \rho U \cdot \nabla U - \nabla p + \rho g \tag{1}$$

$$\nabla \cdot U = 0 \tag{2}$$

where variables velocity (U) and pressure (p) are defined over space and time with time derivative represented as (U_t). Material properties are given via density (ρ) and viscosity (μ).

The following characteristic scales are used for non-dimensionalization: length L, velocity V, time L/V, pressure $\mu_c V/L$. We may define the following dimensionless variables and differential operators:

$$U^* = \frac{U}{V}, \quad p^* = \frac{L}{\mu_c V}\, p, \quad t^* = \frac{V}{L}\, t, \quad Z^* = \frac{1}{L}\, Z$$

$$\mu^* = \frac{1}{\mu_c}\, \mu, \quad \nabla^* = L\nabla, \quad \frac{D}{Dt^*} = \frac{L}{V}\, \frac{D}{Dt}$$

where μ_c is a reference viscosity. Substitution of the above dimensionless variables and differential operators into Equations (1) and (2) yields the non-dimensional Navier–Stokes equations. Discarding * notation for brevity, such a system may be expressed in the following form:

$$Re\, U_t = \nabla \cdot \left(\frac{\mu}{\mu_c}\, \nabla U \right) - Re\, U \cdot \nabla U - \nabla p + F \tag{3}$$

$$\nabla \cdot U = 0 \tag{4}$$

Here, $Re = \rho L V/\mu_c$, is the non-dimensional group called Reynolds number and the zero-shear-rate viscosity (μ_0) is taken as the characteristic viscosity (μ_c). 'F' is the ratio of Reynolds to Froude number which is defined as $F = \rho L^2 g/\mu_c V$.

A semi-implicit time stepping procedure, namely, a Taylor–Galerkin/pressure-correction finite element scheme [11, 12] is employed to solve the governing equations relating to the conservation of mass and momentum. The Taylor–Galerkin/pressure-correction scheme is a fractional-step method derived through Taylor series expansions in time up to second-order and a two-step predictor–corrector scheme is employed. Governing equations are discretized spatially via a Galerkin finite element method. The flow domain is divided into a tetrahedral mesh. Piecewise-linear interpolation is invoked for pressure and quadratic interpolation for velocity over the finite elements. The algorithm follows closely our previously published work [11, 12]. Here, the generalized Newtonian fluid description is invoked to describe the viscous properties of the material, according to a Carreau–Yasuda model. This model supports shear-thinning properties and is represented through the viscosity function $\mu(\dot{\gamma})$ as

$$\mu(\dot{\gamma}) = \frac{\mu_0 - \mu_\infty}{1 + (\lambda\dot{\gamma})^m} + \mu_\infty \tag{5}$$

The particular material parameters chosen in the present study are $\mu_0 = 1.05$ Pa s, $\mu_\infty = 0.001$ Pa s, $\lambda = 0.083$ s and $m = 0.62$. μ_0 is a limiting viscosity at low shear rates, and μ_∞ is an asymptotic value of viscosity at large shear rates (second Newtonian plateau); $\dot{\gamma}$ is the shear-rate, m is a power-law index and λ is a material constant. This model has been selected based on the rheological characterization of dough samples and some model fluids, namely, 1% CMC, 2% CMC, 3% CMC and 4% CMC [15]. These materials are observed to be shear-thinning and may be fitted to the Carreau–Yasuda model. There is a need for these model-fluids, so that translucency would allow for validation via flow visualization (see below).

Matching on rheological properties with dough samples was ensured and particularly so in shear. In the present study, the flow type (full-filled vessels) is heavily shear-dominated and since no free-surfaces are involved, the interfacial fluid-solid boundary effects are overriden (no wetting/peeling [16]). As such, under the current context, extensional influences are minor, hence justifying the choice of model.

The Taylor–Galerkin algorithm has three fractional-stages per time-step as follows:

Stage 1: From initial velocity and pressure fields, non-divergence-free $U^{n+1/2}$ and U^* fields are calculated via a two-step predictor–corrector procedure. The corresponding equations are solved iteratively by a Jacobi method.

Stage 2: Using U^*, calculate the pressure difference $(p^{n+1} - p^n)$ via a Poisson equation, applying a Choleski method of solution.

Stage 3: Using U^* and pressure difference $(p^{n+1} - p^n)$, determine the divergence-free velocity field U^{n+1} by Jacobi iteration.

Adopting quadratic and linear interpolations, $U(x,t)$ and $p(x,t)$ may be expressed as

$$U(x,t) = U_j(t)\phi_j(x), \quad p(x,t) = p_j(t)\psi_j(x) \tag{6}$$

The equations in fully discrete form may be represented in the following notation:

Stage 1a:

$$\left(\frac{2\,Re}{\Delta t} M + \frac{1}{2} S_u\right)(U^{n+1/2} - U^n) = (-S_u U - Re\, N(U)U + L^t p + \phi_i F)^n \tag{7}$$

Stage 1b:

$$\left(\frac{Re}{\Delta t} M + \frac{1}{2} S_u\right)(U^* - U^n) = (-S_u U + L^t p + \phi_i F)^n - Re\, N(U)U^{n+1/2} \tag{8}$$

Stage 2:

$$K(p^{n+1} - p^n) = \frac{-2}{\Delta t} LU^* \tag{9}$$

Stage 3:

$$\frac{Re}{\Delta t} M(U^{n+1} - U^*) = \frac{1}{2} L^t(p^{n+1} - p^n) \tag{10}$$

where U^n, U^{n+1}, p^n and p^{n+1} are nodal vectors of velocity and pressure at t^n and t^{n+1}, respectively; U^* is an intermediate nodal velocity vector introduced in step 1b; M, S_u, $N(U)$, K and L are mass matrix, momentum diffusion matrix, convection matrix, pressure stiffness matrix and divergence pressure gradient matrix, respectively. The detail on the above matrices in an (r,θ,z) co-ordinate system is given as:

$$M_{ij} = \int_\Omega \phi_i \phi_j \, \mathrm{d}\Omega \tag{11}$$

$$S_u = \begin{bmatrix} S_{11} & S_{12} & S_{13} \\ S_{21} & S_{22} & S_{23} \\ S_{31} & S_{32} & S_{33} \end{bmatrix} \tag{12}$$

$$(S_{11})_{ij} = \mu \int_\Omega \left(2\,\frac{\partial \phi_i}{\partial r}\,\frac{\partial \phi_j}{\partial r} + \frac{1}{r^2}\,\frac{\partial \phi_i}{\partial \theta}\,\frac{\partial \phi_j}{\partial \theta} + \frac{2}{r^2}\,\phi_i \phi_j + \frac{\partial \phi_i}{\partial z}\,\frac{\partial \phi_j}{\partial z} \right) \mathrm{d}\Omega \tag{13}$$

$$(S_{12})_{ij} = (S_{21})^{\mathrm{T}} = \mu \int_\Omega \left(\frac{-1}{r^2}\,\frac{\partial \phi_i}{\partial \theta}\,\phi_j + \frac{1}{r}\,\frac{\partial \phi_i}{\partial \theta}\,\frac{\partial \phi_j}{\partial r} + \frac{2}{r^2}\,\phi_i\,\frac{\partial \phi_j}{\partial \theta} \right) \mathrm{d}\Omega \tag{14}$$

$$(S_{13})_{ij} = (S_{31})^{\mathrm{T}} = \mu \int_\Omega \left(\frac{\partial \phi_i}{\partial z}\,\frac{\partial \phi_j}{\partial r} \right) \mathrm{d}\Omega \tag{15}$$

$$(S_{22})_{ij} = \mu \int_\Omega \left(\frac{2}{r^2}\,\frac{\partial \phi_i}{\partial \theta}\,\frac{\partial \phi_j}{\partial \theta} - \frac{1}{r}\,\frac{\partial \phi_i}{\partial r}\,\phi_j + \frac{\partial \phi_i}{\partial r}\,\frac{\partial \phi_j}{\partial r} + \frac{1}{r^2}\,\phi_i \phi_j - \frac{1}{r}\,\phi_i\,\frac{\partial \phi_j}{\partial r} + \frac{\partial \phi_i}{\partial z}\,\frac{\partial \phi_j}{\partial z} \right) \mathrm{d}\Omega \tag{16}$$

$$(S_{23})_{ij} = (S_{32})^{\mathrm{T}} = \mu \int_\Omega \left(\frac{1}{r}\,\frac{\partial \phi_i}{\partial z}\,\frac{\partial \phi_j}{\partial \theta} \right) \mathrm{d}\Omega \tag{17}$$

$$(S_{33})_{ij} = \mu \int_\Omega \left(\frac{\partial \phi_i}{\partial r}\,\frac{\partial \phi_j}{\partial r} + \frac{1}{r^2}\,\frac{\partial \phi_i}{\partial \theta}\,\frac{\partial \phi_j}{\partial \theta} + 2\,\frac{\partial \phi_i}{\partial z}\,\frac{\partial \phi_j}{\partial z} \right) \mathrm{d}\Omega \tag{18}$$

$$L = (L_1, L_2, L_3) \tag{19}$$

$$L_r = \int_\Omega \left(\frac{\phi_i}{r} + \frac{\partial \phi_i}{\partial r} \right) \psi_j \,\mathrm{d}\bar{\Omega} \tag{20}$$

$$L_\theta = \int_\Omega \frac{1}{r}\,\frac{\partial \phi}{\partial \theta}\,\psi_j \,\mathrm{d}\bar{\Omega} \tag{21}$$

$$L_z = \int_\Omega \frac{\partial \phi_i}{\partial z}\,\psi_j \,\mathrm{d}\Omega \tag{22}$$

$$N(U)_{ij} = \int_\Omega \phi_i \phi_k U_k \nabla \phi_j \,\mathrm{d}\Omega \tag{23}$$

$$(K)_{ij} = \int_\Omega \nabla \psi_i \nabla \psi_j \,\mathrm{d}\Omega \tag{24}$$

where $\mathrm{d}\Omega = r\,\mathrm{d}r\,\mathrm{d}\theta\,\mathrm{d}z$; $i, j, k = 1, 2, 3$. After solving for velocities and pressure in the flow field, shear-rate ($\dot{\gamma}$), extension-rate ($\dot{\varepsilon}$), rate-of-work done ($\dot{w}$) and torque (T_q) are computed, using the relationships:

$$\dot{\gamma} = 2\sqrt{I_2}, \quad \dot{\varepsilon} = \frac{3I_3}{I_2}, \quad I_2 = \frac{1}{2}\,\mathrm{trace}(D^2), \quad I_3 = \det(D) \tag{25}$$

Here, I_2 and I_3 are the second and third invariants of the rate-of-strain tensor (D), where

$$D = \frac{\nabla u + \nabla u^t}{2} = \frac{1}{2}\begin{bmatrix} 2\dfrac{\partial u_r}{\partial r} & \dfrac{1}{r}\dfrac{\partial u_r}{\partial \theta} - \dfrac{u_\theta}{r} + \dfrac{\partial u_\theta}{\partial r} & \dfrac{\partial u_r}{\partial u_z} + \dfrac{\partial u_z}{\partial u_r} \\ \dfrac{\partial u_\theta}{\partial r} + \dfrac{1}{r}\dfrac{\partial u_r}{\partial \theta} - \dfrac{u_\theta}{r} & 2\left(\dfrac{1}{r}\dfrac{\partial u_\theta}{\partial \theta} + \dfrac{u_r}{r}\right) & \dfrac{\partial u_\theta}{\partial z} + \dfrac{1}{r}\dfrac{\partial u_z}{\partial \theta} \\ \dfrac{\partial u_z}{\partial r} + \dfrac{\partial u_r}{\partial z} & \dfrac{1}{r}\dfrac{\partial u_z}{\partial \theta} + \dfrac{\partial u_\theta}{\partial z} & 2\dfrac{\partial u_z}{\partial z} \end{bmatrix} \tag{26}$$

$$\dot{w}(t) = \int_\Omega (\tau : \nabla U)\, \mathrm{d}\Omega = P_w \tag{27}$$

$$(\tau : \nabla U) = \frac{1}{2}\mu\left(\frac{\mathrm{d}U_i}{\mathrm{d}X_j} + \frac{\mathrm{d}U_j}{\mathrm{d}X_i}\right)^2 = \dot{w}(t,x) \tag{28}$$

$$P_w = T_q \omega \tag{29}$$

Above, P_w is the power, τ the stress tensor, U the velocity vector, Ω the fluid volume, t the time and ω the rotational speed of the vessel per second. Localized rate-of-work done, $\dot{w}(t,x)$, may be interpreted as the integrand of Equation (27).

3. PROBLEM SPECIFICATION

Three types of stirring configurations are considered. With one stirrer, this may be placed in either concentric or eccentric location with reference to the central (vertical) axis of the vessel. A third instance is one with two stirrers. This is an analogue of the one-stirrer eccentric case, where the second stirrer is positioned symmetrically opposite to the first across the vessel. The fluid is driven by the outer vessel wall and fixed at the top of the vessel by a lid, as illustrated in Figures 1(a)–1(b). The computer program developed, based on the above mentioned algorithm, agrees with the analytical solution [17] for flow in a rotating cylinder with a concentric stirrer. Finite element solutions for velocity and pressure are found to be within 0.1%. The concentric scenario was introduced in order to validate the computer code against the background theory.

Finite element meshes of tetrahedral elements are employed in three-dimensions. To construct such meshes, first each brick element is formed, which is then subdivided into six tetrahedra. The height of the vessel is divided into five uniform layers. For the vessel with one stirrer, the horizontal plane is divided into 120 quadrilaterals, see Figure 2(c). This leads to 3600 tetrahedral elements, 5720 velocity nodes and 840 pressure nodes, resulting in a total of 18 000 degrees of freedom. For the vessel with two stirrers, the horizontal plane is divided into 280 quadrilaterals, see Figure 2(d). Correspondingly, this leads to 8400 tetrahedral elements, 13 145 velocity nodes and 1902 pressure nodes, and a total of 41 337 degrees of freedom. The typical three-dimensional meshes and their two-dimensional cross-sectional views for one and two-stirrer cases are shown in Figures 2(a)–2(d).

Initial conditions are taken either from rest for Newtonian low-*Re* flows, or for inelastic fluids as the equivalent Newtonian, steady-state solution. Continuation through *Re* may be

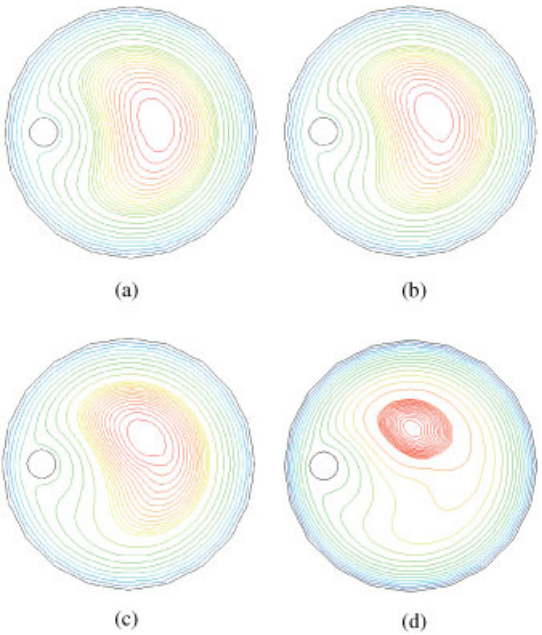

Plate 1. Streamlines for one-stirrer geometry. (a) $Re = 2$, max $= 1.60$; (b) $Re = 4$, max $= 1.52$; (c) $Re = 8$, max $= 1.36$ and (d) $Re = 16$, max $= 1.10$.

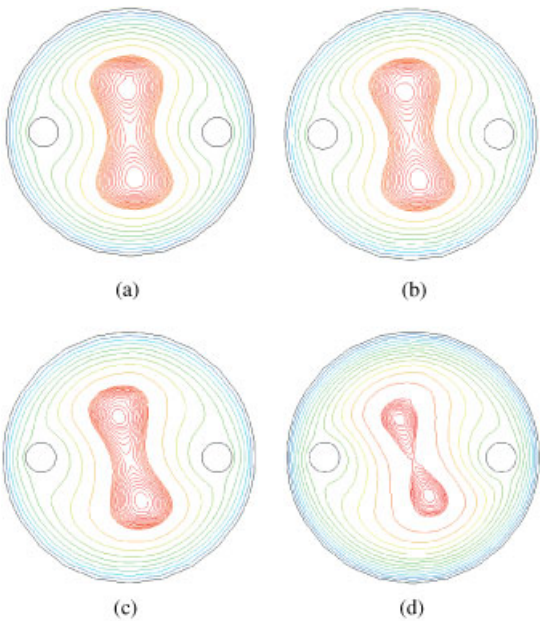

Plate 2. Streamlines for two-stirrer geometry. (a) $Re = 2$, max $= 1.17$; (b) $Re = 4$, max $= 1.15$; (c) $Re = 8$, max $= 1.12$ and (d) $Re = 16$, max $= 1.07$.

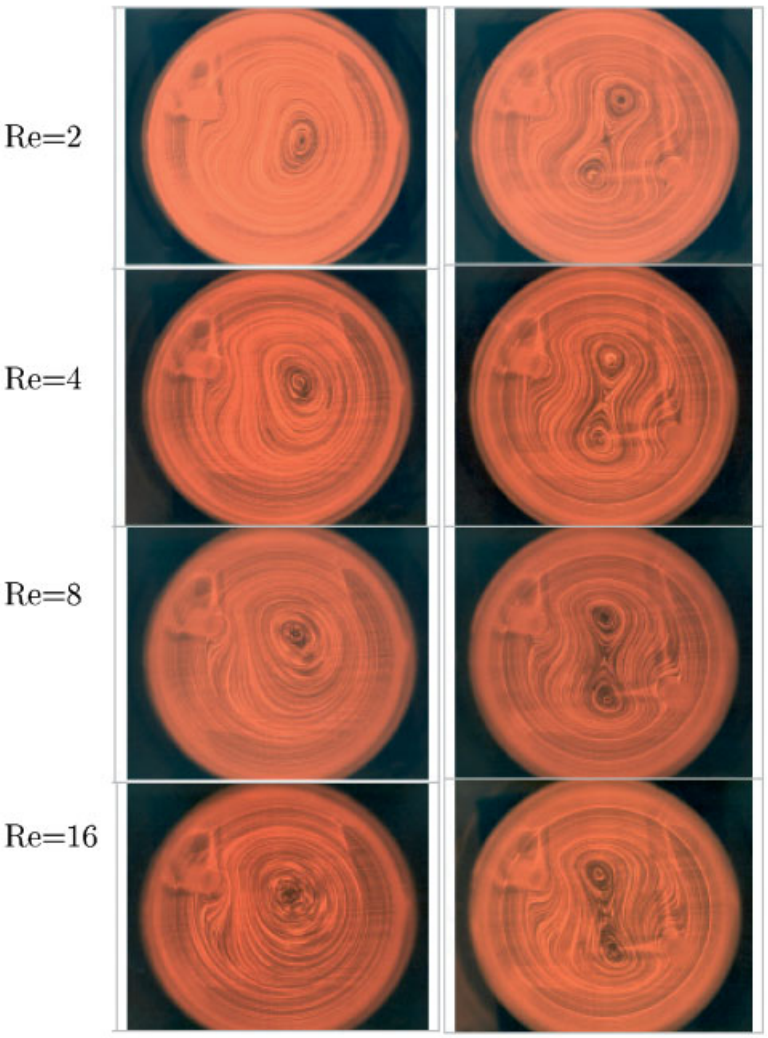

Plate 3. Experimental streaklines for one- and two-stirrer cases (mid-plane).

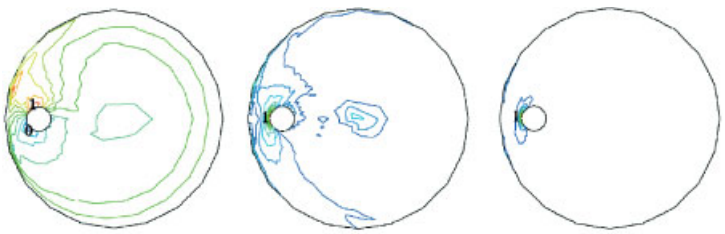

Plate 4. Contours of P, $\dot{\gamma}$ and $\dot{w}$ for single stirrer geometry. (a) $-96.0 < P < 56.0$; (b) $0.96 < \dot{\gamma} < 98.0$ and (c) $0.0 < \dot{w} < 0.041$.

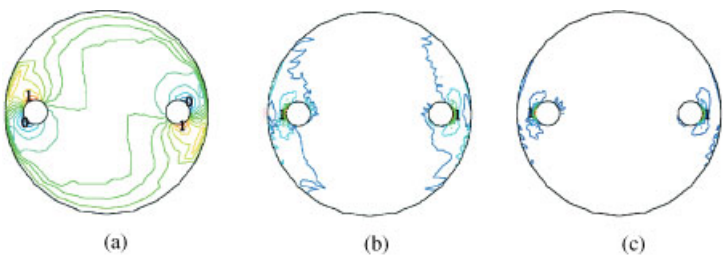

Plate 5. Contours of P, $\dot{\gamma}$ and $\dot{w}$ for two-stirrer geometry. (a) $-89.0 < P < 55.5$; (b) $0.68 < \dot{\gamma} < 93.6$ and (c) $0.0 < \dot{w} < 0.037$.

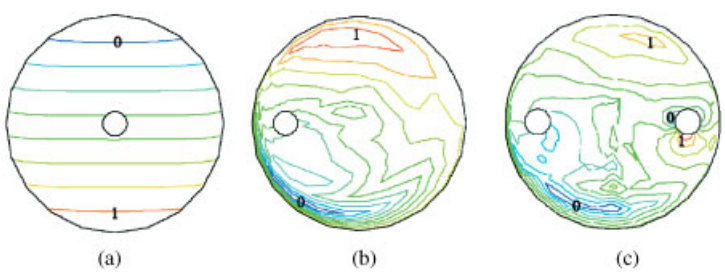

Plate 6. Contours of pressure in horizontal orientation. (a) $-833.0 < P < 936.0$; (b) $-946.8 < P < 322.31$ and (c) $-946.2 < P < 321.7$.

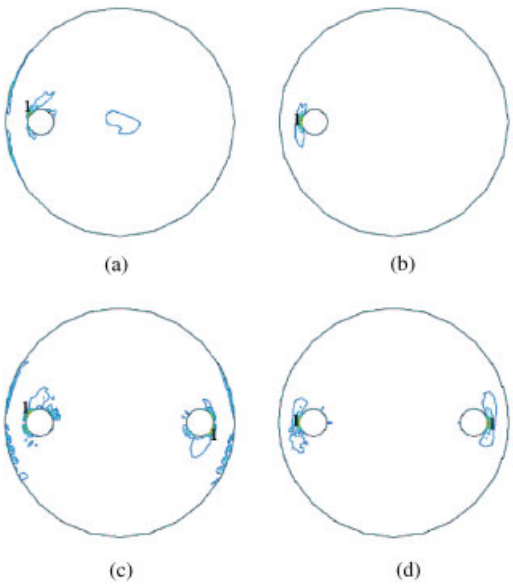

Plate 7. Contours of $\dot{w}$ due to extension and shear for one- and two-stirrer geometries. (a) $0.0 < \dot{w}(\varepsilon) < 0.016$; (b) $0.0 < \dot{w}(\gamma) < 0.035$; (c) $0.0 < \dot{w}(\varepsilon) < 0.014$ and (d) $0.0 < \dot{w}(\gamma) < 0.037$.

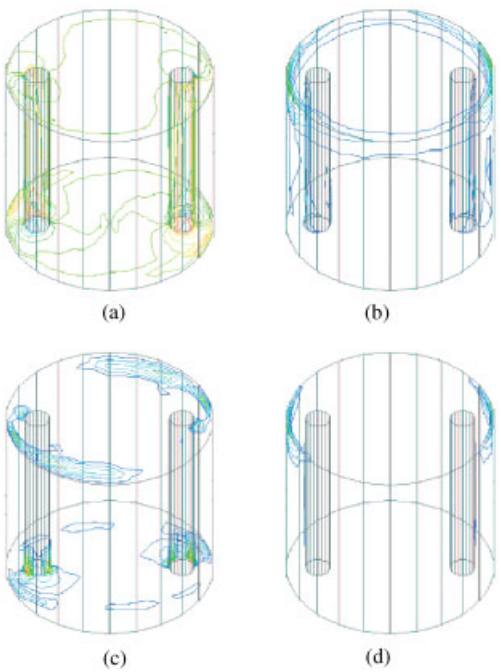

Plate 8. Contours of P, $\dot{\gamma}$, $\dot{\varepsilon}$ and $\dot{w}$ for two-stirrer geometry, in 3D-mode. (a) $-89.0 < P < 56.0$; (b) $0.7 < \dot{\gamma} < 94.0$; (c) $0.0 < \dot{\varepsilon} < 1.71$ and (d) $0.0 < \dot{w} < 0.037$.

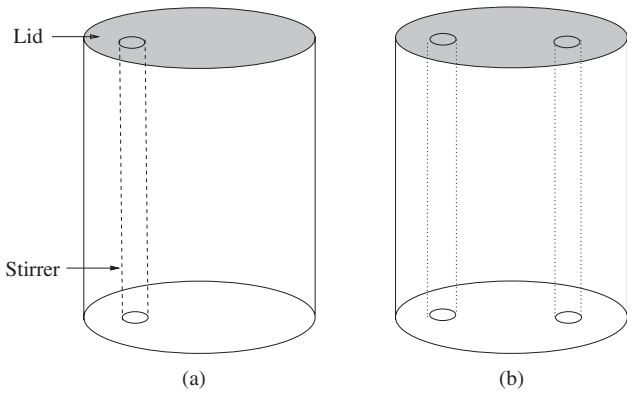

Figure 1. Vessel with one and two stirrers.

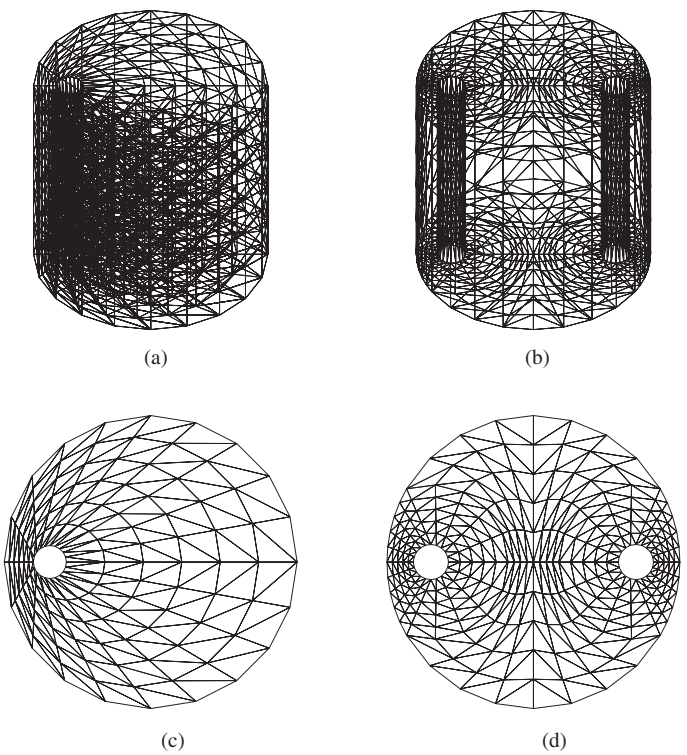

Figure 2. Meshes for one- and two-stirrer problems.

employed subsequently for any particular material. Typically, a time step of $\Delta t = 10^{-2}$ and time-stepping convergence tolerance ε of 10^{-6} are employed, where $\|\chi^{n+1} - \chi^n\|/1 + \|\chi^{n+1}\| < \varepsilon$, for solution nodal vector χ^n at time step n.

4. RESULTS AND DISCUSSION

Numerical simulations for the above two types of mixer designs have been conducted at various speeds for inelastic materials. The findings reflect close agreement against equivalent experimental observations [15, 18, 20, 21]. Most of the results are plotted in a two-dimensional cross-section at a mid-height to give some feel for the problem. For the two-stirrer case, contours of pressure, shear-rate, extension-rate and rate-of-work done are also presented in three-dimensional form, since some patterns, for example, extension-rates vary considerably in the third dimension.

Plates 1 and 2 illustrate typical solution contours of streamline patterns for different speeds, namely, 12.5, 25, 50 and 100 rpm. These are equivalent to Reynolds number settings of 2,4, 8 and 16 for one and two-stirrers, respectively. For the one-stirrer case, a central vortex evolves in opposite juxtaposition to the stirrer at low speed ($Re = 2$). The pattern of flow is seen to twist counter-clockwise away from the horizontal axis, through the centre of the stirrer as speed of rotation (counter-clockwise) increases. With increase in speed, the pattern of flow is seen to contort and twist in an asymmetrical fashion. With the two-rod geometry, a pair of vortices emerge at the centre, driven by separating flow around each stirrer. Again, the flow pattern is seen to contort and twist in an asymmetrical fashion, in anti-clockwise direction as the speed of rotation is increased. The maximum contour levels recorded occur at the centre of the vortex and represent vortex intensity. It is noted that the vortex intensity decreases with increase in speed, pushing the eddy outwards towards the vessel-wall. Streaklines obtained from laser scatter flow visualization data for equivalent Reynolds numbers, with one and two stirrer cases are depicted in Plate 3. The change in vortex-centre positions are measured, both in experiment and simulation, as speed increases from $Re = 2$ to 16. A typical comparison of vortex-centre azimuthal shift, from the horizontal reference line through vessel centre and stirrers, is demonstrated in Table I. This data is for a two-stirrer scenario at 80% of the height of the vessel. The agreement between experiment and prediction is observed to be $O(1\%)$.

Plates 4(a)–4(c) illustrate typical solution contours of pressure, shear-rate and localized rate-of-work done, for the one-stirrer geometry, whereas Plates 5(a)–5(c) depict solution contours of pressure, shear-rate and localized rate-of-work done for the two-stirrer problem depicted in a two-dimensional slice. The positions where maximum and minimum occur are indicated by '1' and '0', respectively. The corresponding values are provided in the figure legend in dimensional quantities. As the vessel rotates in the counter-clockwise direction, the fluid gets compressed on entry to the constricted region between stirrer and vessel, and hence, the maximum pressure arises in this region. When the fluid emerges at the exit from the gap section, the flow expands, and hence, the minimum pressure peaks here. With increasing

Table I. Comparison of vortex-centre azimuthal positions for two-stirrer case.

Reynolds number	θ_{exp}	θ_{sim}
$Re = 2$	100	95
$Re = 4$	110	106
$Re = 8$	116	112
$Re = 16$	125	122

speed, the pressure differential grows, showing greater minimum pressure on the backside of the stirrer. This is a similar situation to that found for flow response past cylinders in a channel. Similar comments with respect to solution contours of pressure and its localized characteristics, carry over from the one-stirrer instance to apply equally for the two-stirrer case. For the two-stirrer instance, a noticeable new feature emerges. That is, the presence of the second stirrer renders a symmetrical solution structure. So, for example, there is a replicated pattern about each stirrer with respect to upstream and downstream (pre- and post-nip-gap) flow as seen in Plates 5 and 8.

Simulations are conducted with the axis of the mixer being horizontal, where body force in the y direction is significant. The pressure patterns differ significantly between horizontal- and vertical-orientations. This may be explained through the fact that the body force acts as a pseudo-pressure gradient, and in this manner, is linked to the pressure as illustrated in Plates 6(a)–6(c). However, the flow kinematics remain as in the vertical-orientation. For the simple concentric scenario, the pressure contours in the vertical-orientations form concentric circles around the stirrer, the maximum pressure on the outer vessel surface and minimum around the stirrer. When the concentric geometry is in the horizontal-orientation, the pressure contours are straight lines parallel to the horizontal central axis through the stirrer as demonstrated in Plate 6(a). In the horizontal-orientation, the body force acts vertically downwards (in the Y direction) and hence the pressure tends to be maximum at the bottom part of the geometry. When the stirrer is placed in eccentric position with respect to the axis of the vessel, as seen in Plates 6(b) and 6(c), the maximum pressure peaks at the upper part of the geometry. This is the region where the fluid experiences compression because of the anti-clockwise direction of rotation of the vessel. The reverse scenario is observed when the direction of rotation is changed from counter-clockwise to clockwise. In the non-concentric cases, the flow kinematics dominates the body force and hence, the maximum is observed in the flow zone prior to the stirrers where the fluid gets compressed and the minimum in the region post-stirrer where it expands. Similar structure is observed in the two-stirrer instance, with symmetry introduced about the stirrers.

In the two-dimensional horizontal slice shown in Plates 4(b) and 4(c), maximum values of shear-rate and rate-of-work done are observed in the narrow region between the vessel and the stirrer. Since the stirrer is stationary and the vessel is rotating, velocity gradients peak around the stirrer, particularly in the constricted gap section between the stirrer and the vessel wall. Hence, more shearing and stretching of the fluid occurs in this region and the rate-of-work done peaks to a maximum there. In a qualitative sense, the total rate-of-work can be segregated into shear and extension components, respectively, as depicted in Plates 7(a)–7(d) for the two geometries. That is, associating extension and shear aligned with the orthogonal cylindrical coordinate system. From these figures, it is apparent that the contours of rate-of-work done due to shear concentrate at the centre of the narrow-gap between the stirrer and the vessel, whereas the contours of rate-of-work done due to extension spread around the stirrer. For the one-stirrer case, the extensional rate-of-work contribution peaks at about one-half of that due to shear at entry to the narrow-gap between the stirrer and the vessel, see Plates 7(a) and 7(c). In the two-stirrer instance, the extensional rate-of-work peak is about one third of that due to shear. Hence, greater extensional work can be attributed to the one-stirrer version and it is this portion that is perceived to maximize build-up of material structure through kneading. The clear preference is therefore established of the mixer design with an asymmetric stirrer option.

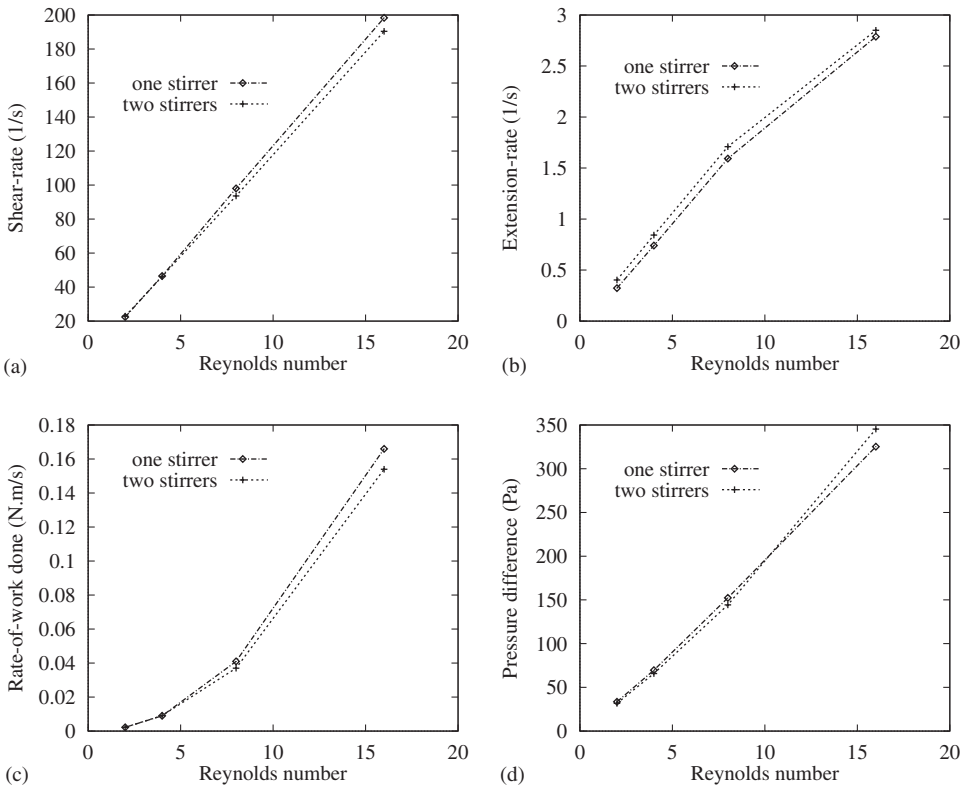

Figure 3. Variation of $\dot{\gamma}$, $\dot{\varepsilon}$, $\dot{w}$ and P with Re for one and two-stirrer designs.

Plates 8(a)–8(d) illustrate solution contours of pressure, shear-rate, extension-rate and localized rate-of-work done shown in three-dimensional mode. From Plate 8(b) and 8(d), maximum shear-rate and rate-of-work done occur at the top periphery of the vessel, mainly in the gap between the stirrer and the vessel. Since the top-lid is stationary and the vessel is rotating, velocity gradients are high in this region and hence rate-of-work done peaks here. From Plate 8(c), extension is deemed to occur at the flow exit near the top and bottom-plates. At the top-plate, extension-rate is higher at the flow exit after the gap between the stirrer and the vessel. As the fluid passes through the gap section, getting squeezed at the entry, expands and stretches at the exit, showing high extension-rates. The stretching which occurs in the vicinity of the stirrer, spreads further and expands over the entire flow field as shown in Plate 8(c). The stationary top-plate enhances stretching and thus extension-rates. Similarly at the bottom-plate, high extension-rates occur in the region where the fluid emerges from the gap and within a small region around the stirrer. The reason for high extension-rates around the stirrer at the bottom-plate may be attributed to the stretching of the fluid at the contact line between the stationary stirrer and moving bottom-plate. The magnitude of extension-rates are negligibly small elsewhere.

Figures 3(a)–3(d) demonstrate the variation in maxima of shear-rate, extension-rate, rate-of-work and pressure-difference versus Reynolds number for both one- and two-stirrer geometries,

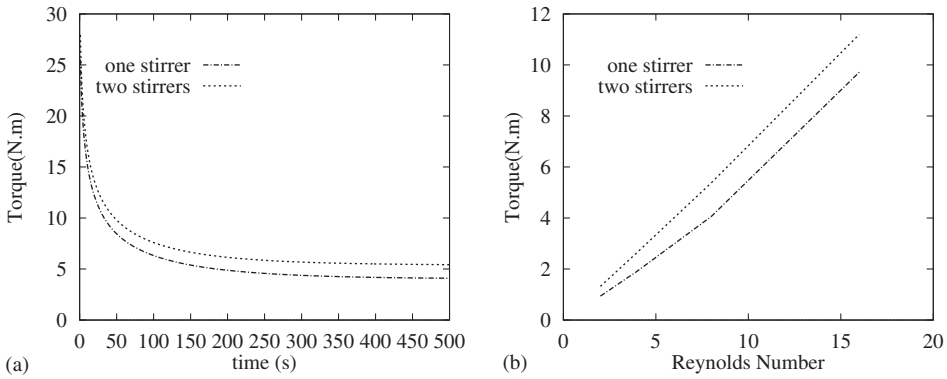

Figure 4. Variation of torque with time and speed.

Table II. Contrast between Newtonian and inelastic materials.

	One-stirrer		Two-stirrer	
Field variables	Newtonian	Inelastic	Newtonian	Inelastic
$\dot{\gamma}$	177	199	168	192
$\dot{w}$	0.192	0.168	0.172	0.156
T_q	4.32	4.06	5.61	5.38

to illustrate the effect of increasing speed. It is apparent that all variables increase with increase in inertia. From these results, it is observed that the introduction of a second stirrer does not alter the magnitude of the rates significantly at low Reynolds numbers. However, as the rotational speed increases, for example $Re > 10$, the difference in these quantities between one- and two-stirrer geometries, increases as demonstrated in Figures 3(a), 3(c) and 3(d).

Figures 4(a) and 4(b) illustrate the variation of torque for one and two-stirrer cases. Figure 4(a) shows the transient variation at $Re = 8$ (50 rpm), whilst Figure 4(b) represents steady-state values at the various speed settings. Torque is a measure of an integrated quantity of rate-of-work done in the whole field. As time progresses from a quiescent state, torque decreases and reaches a constant value as a steady-state is approached. At the onset of motion ($t = 0$), torque is at a maximum due to fluid and stirrer resistance against the vessel motion. For an equivalent speed, the magnitude of torque is 7% higher for the two-stirrer case, at a typical speed setting of $Re = 8$ (50 rpm). There is an increased resistance arising from the presence of a second stirrer. Since the torque reflects the complete field contributions of the rate-of-work done, its magnitude is higher for the two-stirrer flow, above that of the single stirrer case. Similarly as with other variables, torque increases with increasing speed of vessel rotation.

With one and two-stirrer designs, Table II records the contrast between Newtonian and inelastic materials for a typical trial run at a speed of 50 rpm ($Re = 8$). Both trials provide similar results. For an equivalent speed, shear-rate maxima are 20% higher for the inelastic fluid due to shear-thinning. Torque also declines as shear-thinning rheology is introduced. Local rate-of-work maxima and power reduce for inelastic above Newtonian fluids, being dominated by viscous influence. An important observation is that one-stirrer designs lead to

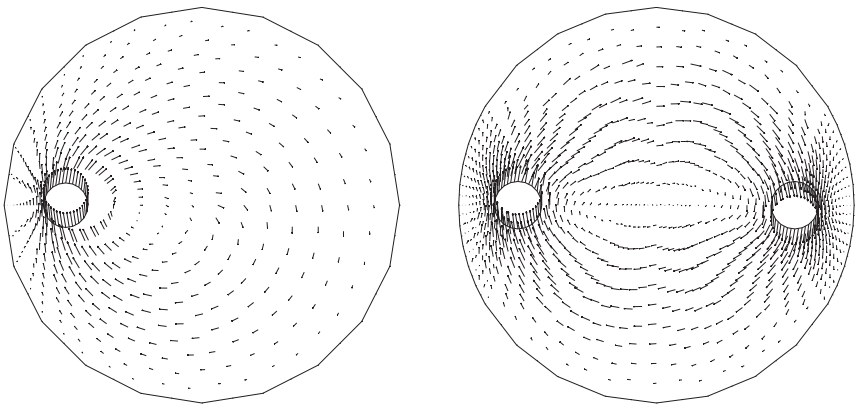

Figure 5. Velocity vector plots for rotating stirrer motion.

enhanced local rate-of-work over two-stirrer alternatives (as much as 13% higher). This would not be apparent from torque calibrations.

Finally, we attempt to relate this process to the actual industrial situation, where the stirrers rotate and the vessel is stationary. This is achieved by translating the motion of the vessel to that of the field. The resulting velocity vectors, at a low inertia setting of $Re = 2$, for both one and two-stirrer scenarios are presented in Figures 5(a) and 5(b). These patterns may be contrasted against the results of Plates 1(a) and 2(a), respectively. The central vortices of the alternative vessel-driven motion are now no longer apparent.

5. CONCLUSIONS

We have successfully demonstrated the use of a numerical flow solver for non-Newtonian fluids as a predictive tool for dough kneading. We have been able to provide physically realistic simulations for these complex rotating flows. The contrast between one- and two-stirrer scenarios, and the changes in flow pattern with speed, have been validated against equivalent experimental findings. Two-stirrer solutions display certain aspects of symmetry, above their one-stirrer counterparts. The shear-rates, pressures and rate-of-work done are localized in extrema in the neighbourhood of the stirrers. Maxima in shear-rate correspond to that in rate-of-work done at the narrowest part of the nip-gap between stirrer and vessel. Extension-rates are maximum at flow exit near the top and bottom-plates. The maximum in local rate-of-work is higher for the single-stirrer, as opposed to the two-stirrer geometry. However, the torque and power consumption are higher for the two-stirrer case. Increase of vessel rotation speed, elevates inertia, twists vortex patterns and increases shear-rate, pressures, rate-of-work done and torque. Greater extensional work is observed for the mixer with the one-stirrer design. A comparative study between Newtonian and inelastic fluids yields higher shear-rates and lower rate-of-work, torque and power for inelastic materials. The reverse scenario to the vessel rotating demonstrates the actual industrial situation.

In related work [19], we go further and address part-filled scenarios in two and three dimensions and the phenomena associated with wetting-and-peeling boundary contact. There,

an arbitrary Lagrangian–Eulerian method is used to deal with free-surfaces. Elsewhere [13, 14], more complicated material representation is incorporated, so that systems are introduced which more closely reflect the properties of dough (viscoelastic).

ACKNOWLEDGEMENTS

Financial support for this work, from BBSRC (Grant No: 58/D08174), RHM Research, United Biscuits, Pilsbury Co., Mono Equipment and Sasib Bakeries, is acknowledged. The support work of Dr D. Ding during this project is also gratefully acknowledged.

REFERENCES

1. Beris A, Amstrong RC, Brown RA. Perturbation theory for visco-elastic fluids between eccentric rotating cylinders. *Journal of Non-Newtonian Fluid Mechanics* 1983; **13**:109–148.
2. Xue SC, Phan-Thien N, Tanner RI. Fully three-dimensional, time-dependent numerical simulations of Newtonian and viscoelastic swirling flows in a confined cylinder Part 1. Method and steady flows. *Journal of Non-Newtonian Fluid Mechanics* 1999; **87**:337–367.
3. Atobe T. Lagrangian chaos in the Stokes flow between two eccentric rotating cylinders. *International Journal of Bifurcation and Chaos* 1997; **7**:1007–1023.
4. Kim E. A mixed Galerkin method for computing the flow between eccentric rotating cylinders. *International Journal for Numerical Methods in Fluids* 1998; **26**:877–885.
5. Dai RX, Dong Q, Szeri AZ. Flow of variable-viscosity fluid between eccentric rotating cylinders. *International Journal of Non-linear Mechanics* 1992; **27**:367–389.
6. Andres AS, Szeri AZ. Flow between eccentric rotating cylinders. *Journal of Applied Mechanics*, *Transactions of the ASME* 1984; **51**:869–878.
7. Prakash S, Kokini JL. Estimation and prediction of shear rate distribution as a model mixer. *Journal of Food Engineering* 2000; **44**:135–148.
8. Prakash S, Kokini JL. Determination of mixing efficiency in a model food mixer. *Advances in Polymer Technology* 1999; **18**:145–152.
9. Prakash S, Karwe MV, Kokini JL. Measurement of velocity distribution. In the Brabender Farinograph as a model mixer, using Laser-Doppler Anemometry. *Journal of Food Process Engineering* 1999; **22**:435–454.
10. Bolksma AH. Theoretical aspects of Farinograph. In *The Farinograph Handbook*, D'Appolonia BL, Kunerth WH (eds). American Association of Cereal Chemistry: St. Paul, MN, 1982, 7–10.
11. Hawken DM, Tamaddon-Jahromi HR, Townsend P, Webster MF. A Taylor–Galerkin-based algorithm for viscous incompressible flow. *International Journal for Numerical Methods in Fluids* 1990; **10**:327–351.
12. Ding D, Townsend P, Webster MF. On computations of two and three-dimensional unsteady thermal non-Newtonian flows. *International Journal for Numerical Methods in Heat Fluid Flow* 1995; **5**:495–510.
13. Baloch A, Grant PW, Webster MF. Parallel computation of two-dimensional rotational flows of viscoelastic fluids in a cylindrical vessel. *Engineering Computations* 2002; **19**:820–853.
14. Baloch A, Webster MF. Distributed parallel computation for complex rotational flows of non-Newtonian fluids. *International Journal for Numerical Methods in Fluids* 2003; at press.
15. Binding DM, Couch MA, Sujatha KS, Webster MF. Experimental and numerical simulation of dough kneading in filled geometries. *Journal of Food Engineering* 2003; at press.
16. Sujatha KS, Webster MF, Couch MA, Binding DM. Modelling and experimental studies of rotating flows in part-filled vessels: wetting and peeling. *Journal of Food Engineering* 2003; **57**:67–79.
17. Bird RB, Stewart WE, Lightfoot EN. *Transport Phenomena*. Wiley International Edition: New York, 1960.
18. Couch MA, Binding DM. Experimental Simulation of Dough Kneading. In *Proceeding of XIII International Cong. on Rheology*, vol. 2. British Society of Rheology: Cambridge, UK, 2000; 351–353.
19. Webster MF, Ding D, Sujatha KS. Modelling of free-surface in two and three-dimensions. In *Proceeding of Moving Boundaries*-2001, WIT, Lemnos, Greece, 2001; 102–111.
20. Ding D, Webster MF. Three-dimensional numerical simulation of dough kneading. In *Proceeding of XIII International Cong. on Rheology*, vol. 2. British Society of Rheology: Cambridge, UK, 2000; 318–320.
21. Sujatha KS, Ding D, Webster MF. Modelling three-dimensional mixing flows in cylindrical-shaped vessels. In *Proceeding of ECCOMAS*-2001, Swansea, UK 2001.

